Pergamon

Computers & Fluids Vol. 27, No. 1, pp. 29–46. 1998

Printed in Great Britain
PII: S0045-7930(97)00025-X
0045-7930/98 $19.00 + 0.00

SOME PHYSICAL INSIGHTS INTO A TWO-ROW FINNED-TUBE HEAT TRANSFER

S. F. TSAI and TONY W. H. SHEU†

Department of Naval Architecture and Ocean Engineering, National Taiwan University, 73 Chou-Shan Road, Taipei, Taiwan, Republic of China

(Received 16 December 1996; in revised form 10 December 1997)

Abstract—A three-dimensional numerical study was conducted to broaden our knowledge of the conjugate heat transfer in a finned-tube heat exchanger element. A finite volume discretization method and a SIMPLE-based solution algorithm were applied to working differential equations and their discrete counterparts for computation of gas velocities and temperatures. Since the heat transfer between the gaseous and solid phases is determined by the complex flow structure, calculations for three-dimensional thermally and hydrodynamically developing laminar flows are performed by iteratively solving the heat conduction equation for the plate fin and conservation equations for the gas phase via the coupling boundary condition. The emphasis of this study is directed toward numerical exploration of the flow structure. To this end, the underlying topological theory shows the promise of being a powerful tool for the study of flow details. In dry conditions, some insight in the heat-transfer capability of the two-row finned-tube heat exchanger can be gained by examining the span-averaged Nusselt number and span-averaged pressure drop in the flow passage.

1. INTRODUCTION

Heat transfer in finned-tube exchangers constitutes a conjugate problem which finds many engineering applications. Among other examples, applications to air-conditioning systems, air heaters and power stations are of some importance to daily human life. Problems of this type generally involve tubes and plate fins, over which there exists air as the working fluid media. The various fin configurations are characterized as having plain, corrugated, punched and slotted types [1]. Over the years, slotted fins have received an increasing amount of attention in the industrial community. It is for this practical reason that extensive efforts have been devoted to numerical exploration of slotted fins, among which the louvered fin, the Forgo fin, and the radial-strip fin have been frequently referred to in the past two decades [1]. Even though plate-and-fin heat exchangers have been widely used, no experimental method exists that allows accurate measurement of the conjugate local heat transfer [2]. The main cause of experimental difficulty lies in the limiting space between the two adjacent fins of complex geometries. Numerical investigation of this class of problem thus emerges as a substitute for the design of heat exchangers.

The flow structure in the finned-tube configuration can be fairly complex. Flow complexities are primarily attributable to the coexistence of a horseshoe vortex, a stagnant wake behind the tube and, of course, a developing flow along the plate near the leading edge. The presence of the horseshoe vortex, which manifests itself by showing the counter-rotating nature of the longitudinal vortices, aids in the transfer of heat. In contrast, the dead water zone behind the tube is responsible for the poor heat transfer. Given these facts, the flow structure in the channel passage is believed to be extremely complex and plays an influential factor in determining the efficiency of heat transfer. The first step in finding a good design of a finned-tube heat exchanger is to build an analysis model that allows us to explore in depth the flow structure. The recent progress in numerical analyses and advancements in computer hardware have made it feasible to numerically analyze the complex three-dimensional interaction between the wake and horseshoe vortex.

Several numerical studies of finned-tube heat-transfer problems have been carried out [1–7]. Most of these were performed with emphasis placed on the parametric study. These studies have provided us with useful information, revealing that the heat flux to the fin behind the tube was

†Corresponding author.

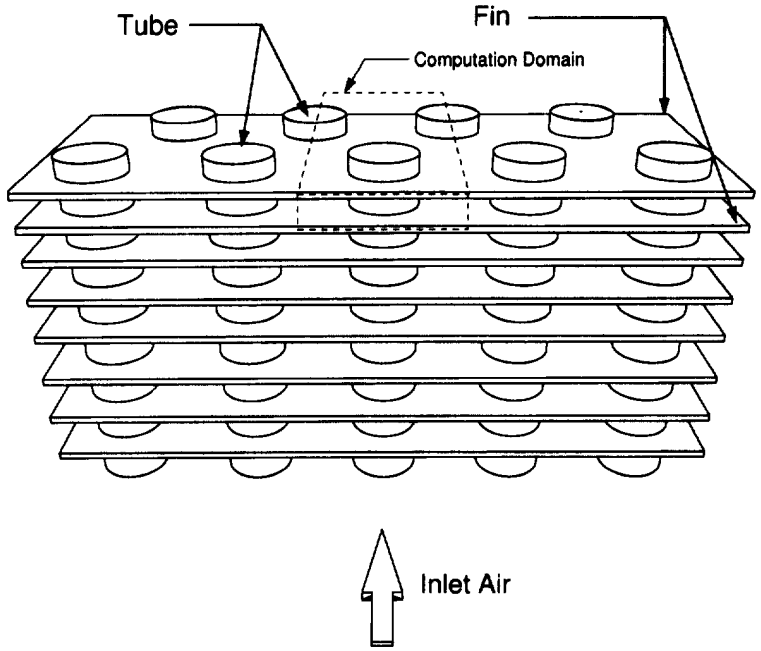

Fig. 1. A schematic illustration of a two-row staggered tubes in a finned-tube heat exchanger.

very low and that the horseshoe vortex formed in front of the tube engenders recirculating flow pattern in a helical vortex format and thus enhanced the heat transfer. Very few studies, to the authors' knowledge, have been directed towards clarifying this flow structure in the fin-tube flow passage. Bearing in mind that the row-fin tube setting, as shown in Fig. 1, represents the basic type of finned-tube heat exchanger, better understanding of this flow passage is definitely crucial to any new design of a high-performance heat exchanger. To this end, a plate fin without perforation is dealt with in this study.

In Section 2, we consider Navier–Stokes equations for the solution of the flow field while energy equation for the temperature field. This is followed by a brief description of the underlying finite volume discretization method, the solution algorithm and the multi-dimensional advective flux discretization scheme. For confident use of the developed computer code for the presently investigated fin-tube heat exchanger problem, validation against analytic data is presented in Section 3. Prior to discussing in detail the complex flow structure, we describe the problem of present interest. In Section 4, attention is given to clarifying the interaction structure of the horseshoe vortex and the wake behind the tube. Plausible reasons for the formation of helical vortices are also addressed. The closing remarks are presented in Section 5.

2. THEORETICAL ANALYSIS

2.1. Mathematical model

We consider air in this article as a working medium. In view of the fact that the Mach number of the air velocity is much less than 0.2, the present analysis can be rationally conducted within the incompressible context. In the absence of an applied body force, a complete set of conservation equations for the flow field is given by the following elliptic–parabolic equations in Ω for a given Reynolds number $Re = UL/\upsilon$:

$$\frac{\partial u_i}{\partial x_i} = 0 \tag{1}$$

$$\frac{\partial u_i}{\partial t} + \frac{\partial}{\partial x_m}(u_m u_i) = -\frac{\partial p}{\partial x_i} + \frac{1}{Re}\frac{\partial^2 u_i}{\partial x_m \partial x_m}. \tag{2}$$

As for the air temperature in the flow passage, it is computed using the following conservation

of energy equation:

$$\frac{\partial T}{\partial t}+\frac{\partial}{\partial x_m}(u_m T)=\frac{1}{Pe}\frac{\partial^2 T}{\partial x_m \partial x_m}. \tag{3}$$

The dimensionless parameter Pe shown in Equation (3) denotes the Peclet number, which is defined as $Pe = Pr \times Re$. Here, Pr is the so-called Prandtl number ($Pr = \upsilon/\alpha$), where α is the thermal diffusivity.

In the literature, we find several sets of working variables to choose from. Among these, we prefer to employ the primitive-variable formulation for this class of flows simply because this variable setting permits specification of closure boundary and initial conditions [8]. Moreover, these closure conditions are relatively easy to implement in the computer code.

2.2. Numerical model

When incompressible flow Equations (1) and (2) are involved, we encounter difficulties regarding numerical instability in situations where advection predominates over diffusion. Prediction errors due to oscillatory velocities plus the so-called false diffusion error can grossly pollute the flow physics over the entire domain. A simple remedy for such discretization errors is to apply the third-order QUICK upwind scheme [9], which is applicable to nonuniform meshes, to approximate advective fluxes. It must be borne in mind that discretization errors arising from use of a one-to-one curvilinear coordinate transformation are considerable. This further causes the prediction accuracy for problems involving highly stretched and distorted meshes to deteriorate. In attempting to explore in depth the flow structure, we conduct analysis in a channel containing a simple set of rectangular grids.

For analysis formulated on a velocity–pressure formulation basis, one has a choice of applying a grid staggering [10] or a collocating [11] strategy to storing working variables. While use of above two grid layouts to suppress node-to-node pressure oscillations has long been recognized in the literature, we abandon the collocating grid approach in favor of the first strategy. Regardless of programming complications, the staggered grid approach outperforms the nonstaggered grid in the sense that the latter approach lacks boundary pressures that are indispensable for analysis involving a Poisson-type pressure-correction equation. On the control surface of a finite volume cell, each primitive variable takes over a node to itself, whereas the pressure node is surrounded by nodal velocities. This variable setting permits use of the finite volume integration method to discretize each conservation equation under these circumstances.

2.3. Solution algorithm

In simulating incompressible fluid flows, it is essential to assure satisfaction of discrete divergence-free velocities. While use of a mixed formulation meets this constraint condition, we encounter a much larger discrete system. The need to avoid excessive demand for computer storage has prompted researchers to consider segregated approaches. In the present paper, the solutions to discretization equations are obtained sequentially for all primitive variables. The numerical solutions to Equations (1)–(3) are obtained by following the steps below:

(1) With the user-specified initial values for working variables, the continuity and the momentum equations [Equations (1) and (2)] are iteratively solved using the underlying SIMPLE iterative algorithm [12].

(2) The energy equation [Equation (3)] is then solved with the computed convergent velocities and the assumed temperatures, which are stored at the same point as are those for the pressure.

(3) With the air and fin temperatures computed, we can calculate the local heat flux q by means of

$$q=-\left.\frac{\partial T}{\partial z}\right|_{z=0}+\left.\frac{\partial T}{\partial z}\right|_{z=1}. \tag{4}$$

(4) Given that the thickness of the fin, δ, is negligibly small ($\delta = 0.115$ mm), as compared with the depth of the air passage, H, the temperature variation across the fin can be rationally neglected. As a result, the dimensionless temperature distribution, T_f, on the plate fin can be computed from

$$\frac{\partial^2 T_f}{\partial x^2} + \frac{\partial^2 T_f}{\partial y^2} = \frac{1}{F_i}\dot{q} + \frac{1}{F_t}\frac{\partial T}{\partial t}. \tag{5}$$

In the above equation, the fin efficiency parameter F_i is defined as follows:

$$F_i = \frac{k_f}{k}\frac{\delta}{H}, \tag{6}$$

where k and k_f are thermal conductivities for the gas and the fin, respectively. The other parameter involved in the normalization procedure is known as the damping parameter, which is defined as:

$$F_t = \frac{\alpha_f}{\alpha}\frac{1}{Pe}, \tag{7}$$

where α and α_f are thermal diffusivities for the gas and solid fin, respectively.

(5) We repeat the calculation from step 2 to calculate the energy equation for the gas temperature using the most updated value of T_f as the boundary condition.

(6) The steps, starting from 3 and terminating at step 5, are repeated until the convergent solutions are obtained.

3. VALIDATION STUDY

As a first step in the numerical investigation of the physical problem, we justify our computer code. A validation study is often carried out by conducting an analytical test. To achieve this goal and, furthermore, estimate the spatial rate of convergence of the scheme employed, we consider incompressible Navier–Stokes equations in a simple domain of three dimensions ($-1 \le x$, y, $z \le 1$). The solutions to Equations (1) and (2) are sought in a domain with the following zero-divergence velocity field [13]:

$$u = -a[e^{ax}\sin(ay \pm dz) + e^{az}\cos(ax \pm dy)]e^{-d^2t}$$

$$v = -a[e^{ay}\sin(az \pm dx) + e^{ax}\cos(ay \pm dz)]e^{-d^2t}$$

$$w = -a[e^{az}\sin(ax \pm dy) + e^{ay}\cos(az \pm dx)]e^{-d^2t}. \tag{8}$$

With these analytical specifications of the boundary velocities, the pressure takes the following analytical form:

$$p = -\frac{a^2}{2}[e^{2ax} + e^{2ay} + e^{2az} + 2\sin(ax \pm dy)\cos(az \pm dx)e^{a(y+z)} + 2\sin(ay \pm dz)\cos(ax \pm dy)e^{a(z+x)} + 2\sin(az \pm dx)\cos(ay \pm dz)e^{a(x+y)}]e^{-2d^2t} \tag{9}$$

where $a = d/2 = \pi/4$.

The study, with $Re = 1$, involves specifying an initial condition according to the equations given in Equation (8). We have carried out the computations under conditions of time spacing $\Delta t = 1/160$ and the grid spacings $h = 1$, 2/3, 1/2, 2/5, 1/3 and 2/7. As is usual, we assessed the employed QUICK-type upwind discretization scheme and SIMPLE iteration algorithm by examining the prediction nodal errors. Tests on various grids were conducted to assure that the solution converged. With grid spacings being continuously refined, we could compute the rate of

convergence from the computed L_2 error norms. As the computed finite volume solutions reveal, the rate of convergence for velocities is 1.6 and 1.08 for the pressure [14]. With this success, we are assured that the proposed computer code is applicable to investigation of finned-tube heat-transfer problems.

4. RESULTS AND DISCUSSION

4.1. Problem description and boundary condition specifications

The physical problem under consideration, as configured in Fig. 1, consists of two rows of parallel tubes and plate fins with air as the working media. Close examination of staggered pipes led us to simulate this problem only in part of the region shown in Fig. 1. By applying symmetric and periodic conditions at the truncated boundaries shown in Fig. 2, this simplifies the analysis and thus dramatically reduces the computational domain. For this study, the physical domain is scaled by $L{:}B{:}H = 0.035{:}0.0204{:}0.0014$.

We place the inlet plane upstream of the leading edge of the fin-plate with a length of 0.45 mm. At this inlet plane, velocities and temperature are assumed to be uniformly specified:

$$(u, v, w) = (u_{in}, 0, 0),\ T = T_0 = 300\ \text{K}. \tag{10}$$

To save disk space, the outlet plane must be truncated at a length which is numerically verified as being sufficiently distant from the trailing edge of the fin-plate. For physical reasons, the streamwise gradients at the synthetic outlet are set to be zero:

$$\frac{\partial \underline{\mathbf{u}}}{\partial x} = 0$$

$$\frac{\partial p}{\partial x} = 0$$

$$\frac{\partial T}{\partial x} = 0. \tag{11}$$

On boundaries other than the no-slip walls where zero velocity components are specified, the following periodic boundary conditions hold:

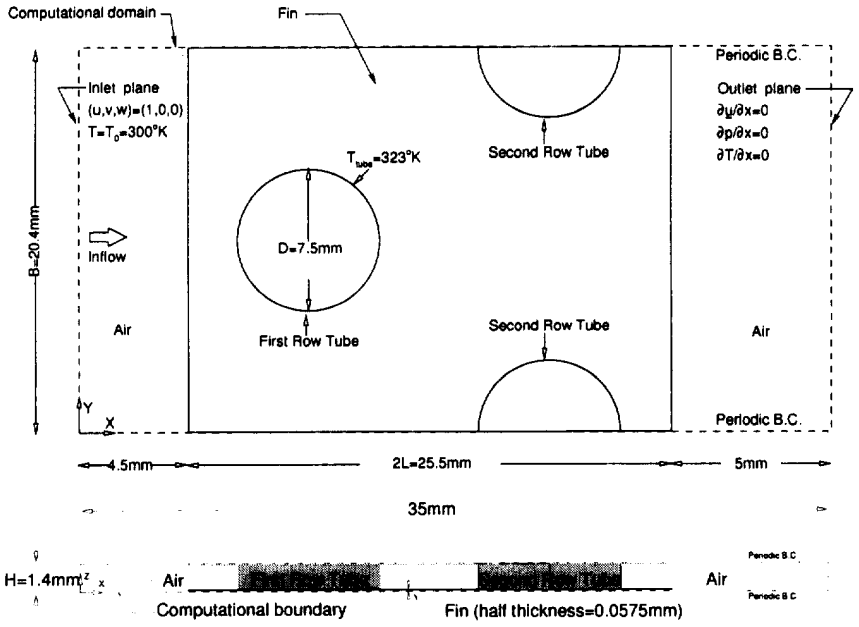

Fig. 2. Description of boundary conditions for velocities and temperature for the investigated problem.

Table 1. Definition of Reynolds number and running flow conditions

$Re = \frac{\dot{m}D_h}{A_c \nu} = \frac{UD_h}{\nu}\frac{A}{A_c}$

$\dot{m}$ = air flow rate

D_h = hydraulic diameter $= (4A_cL)/(A_f + \pi DH/4)$

A_c = minimum flow area of a unit cell

A_f = transfer area for a unit cell

D = tube diameter

L = streamwise length of the channel

H = spacing between plates

A = maximum flow area of a unit cell

U = inlet velocity

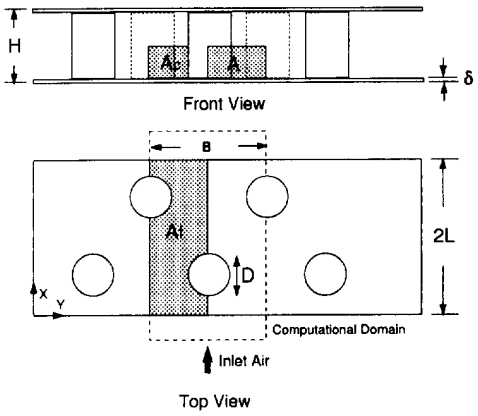

Case	Inlet velocity U (m/s)	Reynolds number
1	0.81	83
2*	1.00	103
3	1.20	124
4*	1.50	155
5	1.81	186
6	2.00	206
7*	2.50	258

*Experimental data are available.

$$\mathbf{u}(x, 0, z) = \mathbf{u}(x, B, z)$$

$$\mathbf{u}(x,y,0) = \mathbf{u}(x, y, H)$$

$$T(x, 0, z) = T(x, B, z)$$

$$T(x, y, 0) = T(x, y, H). \tag{12}$$

On the vertical tube where no-slip conditions need to be specified, the temperature is kept constant. Bearing in mind that velocity and thermal boundary layers may develop over the no-slip wall, grids must be sufficiently stretched to capture high-gradient profiles for hydrodynamical and thermal field variables. For this study, the flow passage is covered with nonuniform grids with a resolution of $142 \times 84 \times 40$. The Reynolds numbers under consideration take on values of 83, 103, 124, 155, 186, 206 and 258. By definition given in Table 1, the Reynolds number involves use of the inlet velocity and the chosen reference length, namely the height H between two fin-plates, the hydraulic diameter and the maximum flow area. In addition, the hydraulic diameter is a function of H, the spanwise length of the channel L, the transfer area for a cell and the minimum flow area of the unit cell shown in Table 1.

4.2. Experimental validation

Even though the employed analysis code has been analytically verified, a question still arises as to whether the algorithmic idea described in Section 2 is applicable to the present simulation. Only the inclusion of a comparison study of computed and experimental data makes it possible to resolve this ambiguity. In the present parametric study, we simply varied the inlet air velocities while keeping the other flow conditions unchanged, leading to Reynolds numbers mentioned in Section 4.1. In accordance with test conditions given in Table 1, experimental calibrations were conducted. Due to lack of space, experimental details are not included in this paper. Our goal is to verify the fluid–thermal coupling model employed and the boundary conditions considered by means of computed and measured pressure drop and Nusselt number.

Figure 3 gives a comparison of pressure drops with varying inlet velocities, starting from 0.81 m/s and terminating at 2.5 m/s, with the measured pressure drops. The agreement between

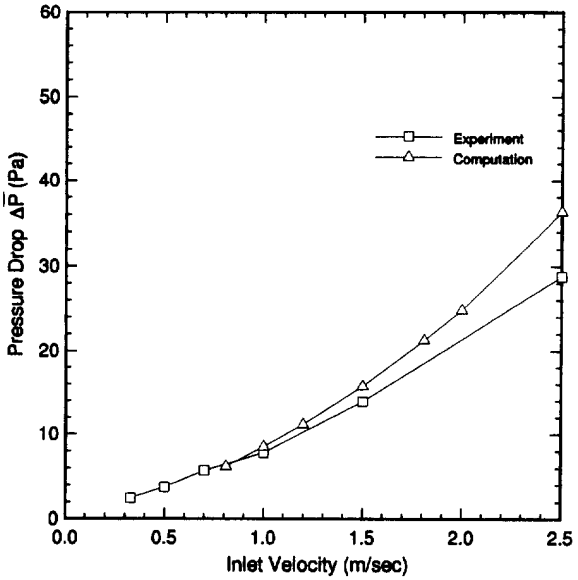

Fig. 3. A comparison study between experimental and computational data for the pressure drop vs test inlet velocities.

the two sets of data is quite acceptable in the trend as well as in the magnitude for inlet velocities less than 1.5 m/s. In the range of present-day encountered air-conditioning machines (0.8–1.5 m/s), the applicability of this computer code is verified. The plot shows that our computed data become increasingly different from the experimental data for Reynolds numbers continuously approaching the transitional flow regime. This may suggest the deficiency of making laminar flow assumption. Refinement of the physical model by incorporating the turbulence model into consideration is left for a subsequent paper. Assessment of the heat transfer is also needed for the sake of completeness. To this end, calibrations were made to study the effect of varying the inlet flow velocities on heat-transfer capability. As Fig. 4 shows, the overall heat-transfer rate increases with the increasing inlet air velocity. As found in Fig. 3, the extent of the deviation between two sets of data becomes considerable only in the flow region which does not fall into the range of Reynolds numbers that is encountered in present-day air-conditioning

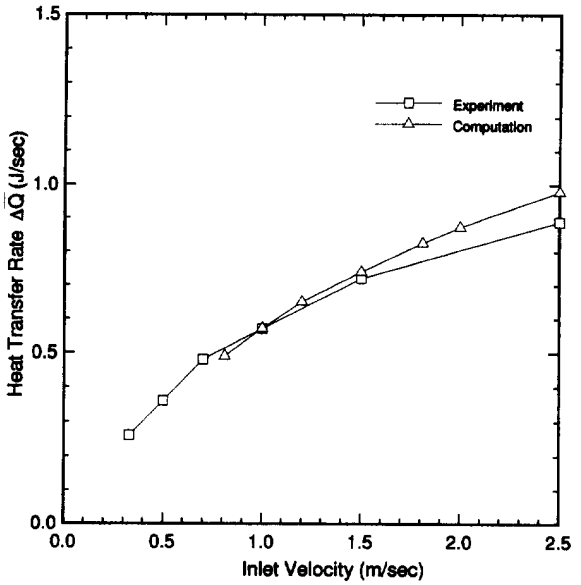

Fig. 4. A comparison study between experimental and computational data for the heat-transfer rate vs inlet velocities.

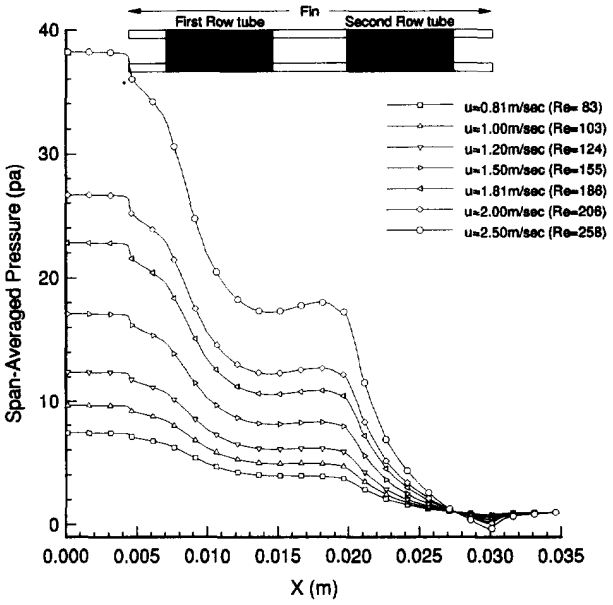

Fig. 5. Span-averaged pressure in the streamwise direction as a function of Reynolds numbers under investigation.

machines. The deviation is, as noted before, believed to be attributable to the fact that turbulence modeling was not included.

With the analysis code analytically verified and the physical model experimentally supported, we have sufficient confidence to explore some physics in the channel passage that is bounded by the two plate fins. Before closing the parametric study on the varying inlet velocities, it is also important to address their effects on some local fluid dynamic and heat-transfer quantities. Chief among the data that help to determine the performance of a heat exchanger are span-averaged pressure and Nusselt number. Figure 5 shows the span-averaged pressure distributions in the streamwise direction. The pressure, averaged in the spanwise sense, decreases slowly as the heat-transfer fin and the vertical tubes are approached. A considerable drop in the span-

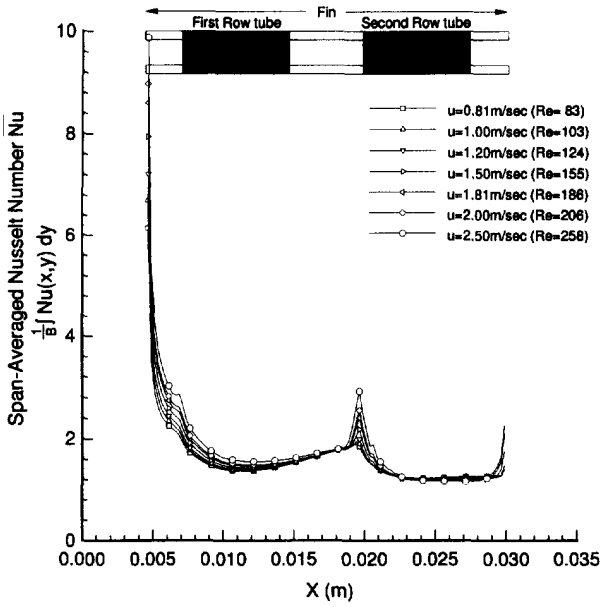

Fig. 6. Span-averaged Nusselt number in the streamwise direction as a function of Reynolds numbers under investigation.

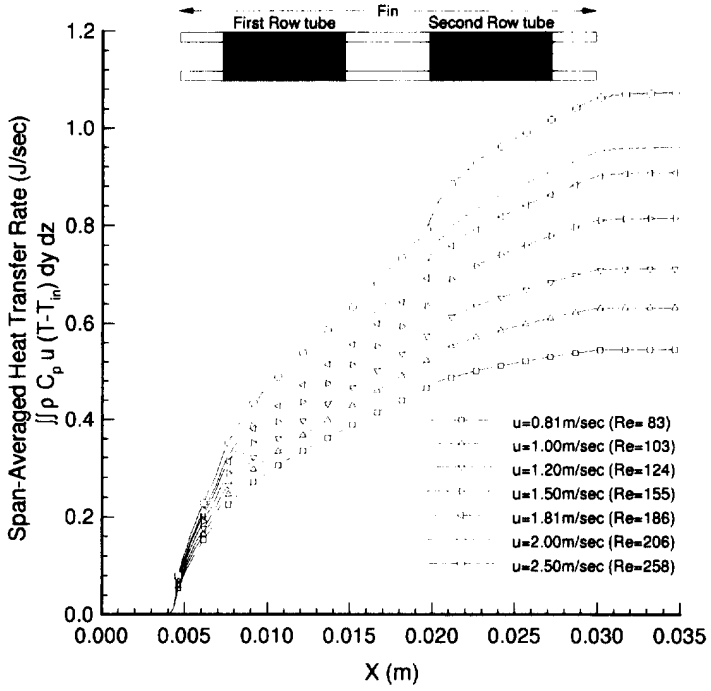

Fig. 7. Span-averaged heat flux $\dot{q}$ in the streamwise direction as a function of Reynolds numbers under investigation.

averaged pressure is found where two rows of vertical tubes are present. It is also noteworthy that there is a mild drop in the pressure as air impinges on the leading edge of the fin-plate. In regions where tubes are located, the degree of the drop in pressure seems not to vary with the inlet Reynolds numbers. In comparison, the slope of the pressure drop in the second row is comparatively larger than that found in the first row.

The effect of the Reynolds number on the heat-transfer capability was also studied. To this end, the span-averaged Nusselt number was chosen as the target for study. Figure 6 plots the Nusselt numbers vs the inlet air velocities, and shows that the larger the inlet velocity, the greater is the heat-transfer rate. For the sake of completeness, we also plot in Fig. 7 the span-averaged heat flux in the streamwise direction as a function of Reynolds numbers. For each

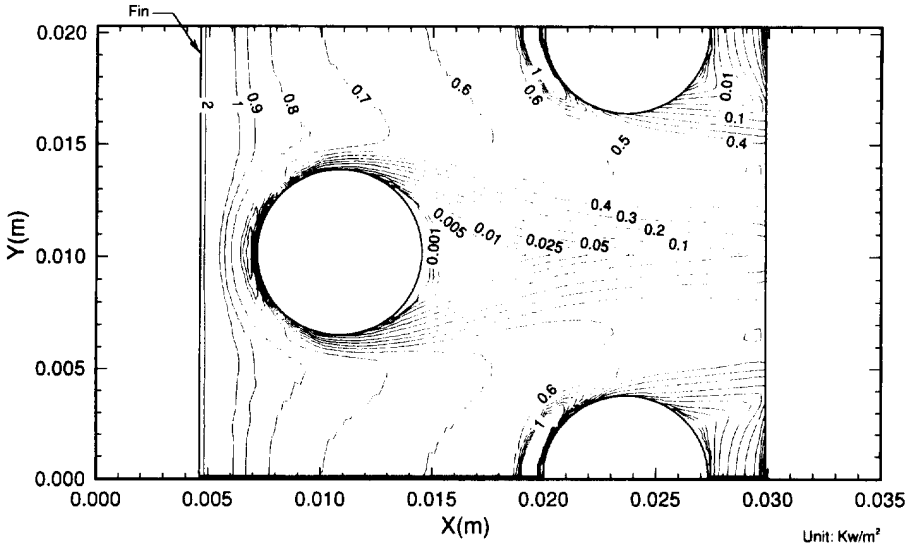

Fig. 8. Heat flux distribution on the fin surface for the case with inlet velocity u = 2.5 m/s.

Reynolds number, the corresponding curve in Fig. 7 is computed by averaging the results shown in Fig. 8. Curves shown in Fig. 7 follow the similar trend in that as the cylinder tube is approached, the heat flux increases in a span-averaged manner. As expected, the larger the inlet velocity, the greater is the span-averaged heat flux.

In the remainder of this section, we will address velocity vector plots to give readers a flavor of the global flow pattern prior to exploring its flow structure. While this goal can be achieved by plotting a direct three-dimensional vector plot for the velocity field, difficulties arise in clearly visualizing the field variables. This prompts us to plot them using two-dimensional plots on the x–z and x–y planes. Due to space considerations, only the case with $u_{in} = 2.5$ m/s is considered and velocity vectors are plotted at some selected planes. In Fig. 9, we plot the (u, v) velocity vectors at fin-plane $z = 0$, as well as at planes $z = H/6$, $H/3$ and $H/2$, which are parallel to the fin-plate. The wake flow pattern behind the vertical cylinder are clearly revealed from these plots; in particular, for those behind the first-row of the tube, the flow separation from the cylinder surface, and the jet-like accelerating flow in the flow passage bounded by two rows of tubes. As Fig. 9 shows, a large-sized flow reversal is clearly seen in the wake region of the second-row tubes. For a clear visualization of this flow reversal, we have placed on the particle paths the top of the u–v velocity vector plots. It is this flow reversal from outlet plane that may have a strong association with the heat-transfer reversal (HTR) phenomenon. This study does not aim to examine under what conditions the heat-transfer reversal will occur.

Figure 10 shows a plane view of the u–w velocity vector plots at three selected planes, $y = 0$, $B/4$ and $B/2$. Inspection of these figures indicates that a boundary layer clearly develops along the fin-plate. At the plane $y = B/4$, where vertical tubes are not encountered, global mass conservation dictates that streamwise velocities of larger amplitudes may prevail. This enhanced convection aids local heat transfer there. In attempting to discuss in more detail of flow patterns present in front of or behind staggered tubes, it is more appropriate to conduct a topological

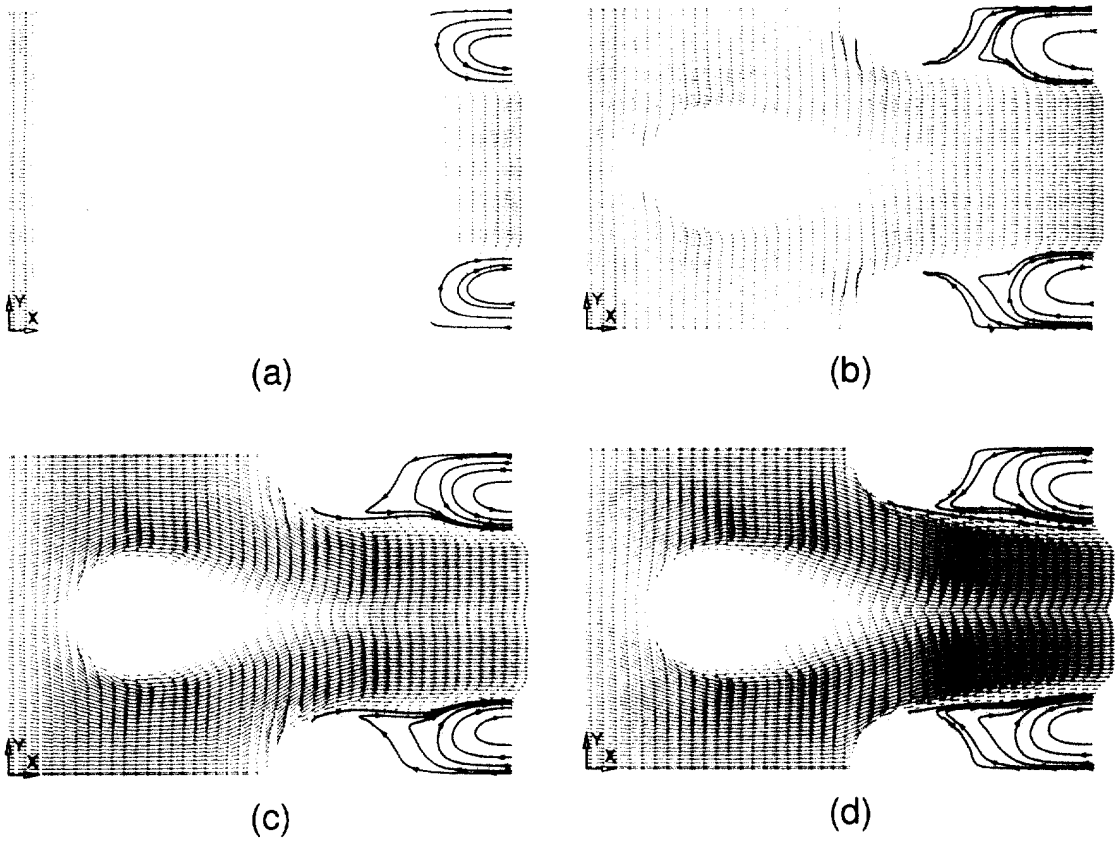

Fig. 9. Velocity vector plots at different z planes: (a) at the fin surface; (b) at $z = H/6$; (c) at $z = H/3$; and (d) at $z = H/2$.

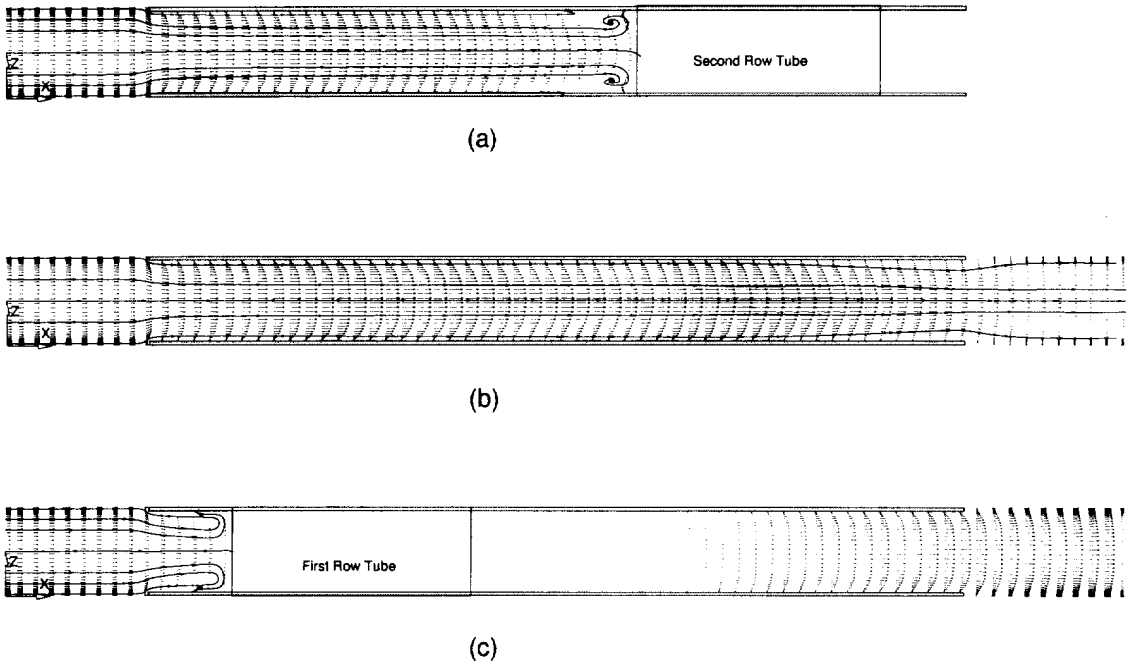

Fig. 10. Velocity vector plots at different y planes: (a) at the $y = 0$ plane; (b) at $y = B/4$ plane; and (c) at $y = B/2$ plane.

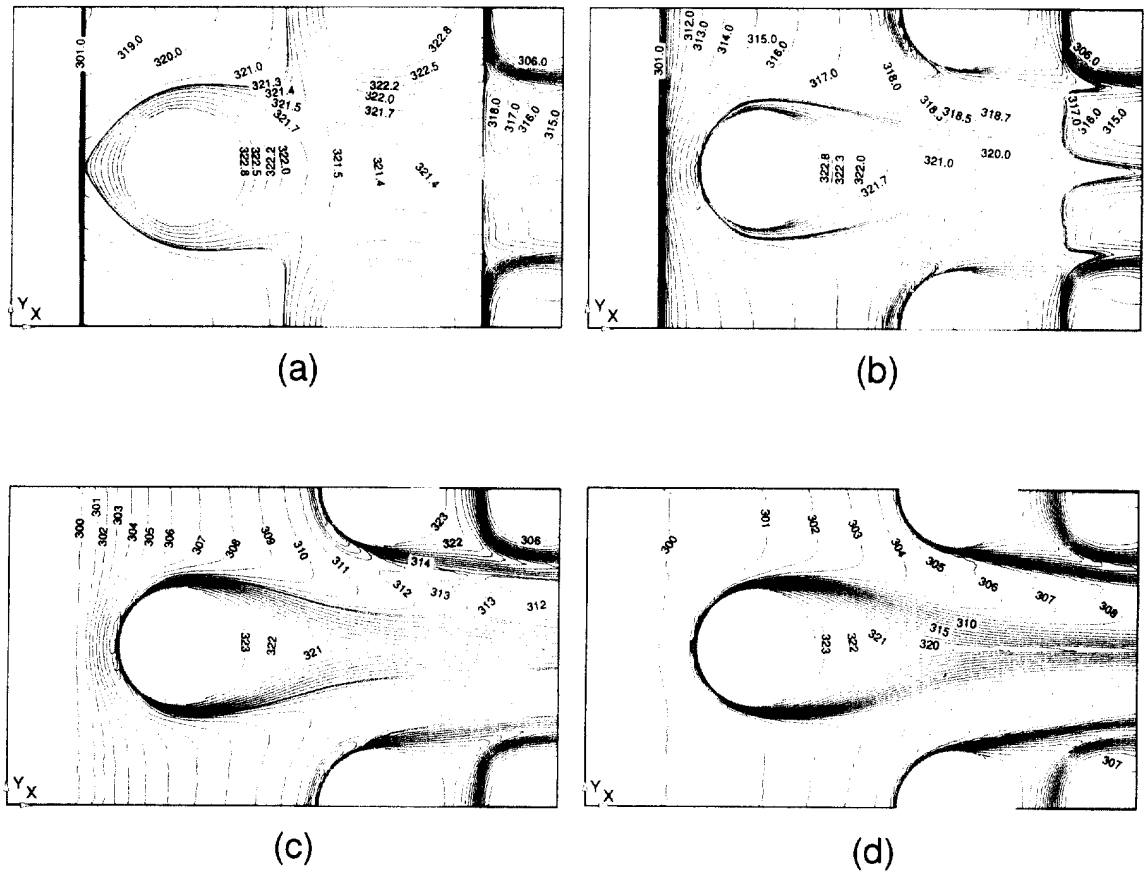

Fig. 11. Temperature contours at different z planes: (a) at $z = 0$; (b) at $z = H/6$; (c) at $z = H/3$; and (d) at $z = H/2$.

study. It is worth noting that the computed velocity vectors at the x–y plane retain flow symmetry with respect to $y = B/2$.

Now that air velocities have been obtained, the associated air temperature can be computed from the energy equation and the coupled boundary condition given in Equation (4). Physical reasons suggest that flows in regions adjacent to the fin surface or in the core of the flow passage are under the influence of convection heat transfer. With the velocity field presented by the fluid dynamic equations, we plot the temperature T_f at the fin surface in Fig. 11(a) and air temperatures in Fig. 11(b–d). The results show that the temperature distribution on the fin surface is much smoother as compared with those in the air passage, reflecting the Poisson nature of the energy equation for the fin given in Equation (5). As the contours of the air temperature show, higher temperature gradients are found in the fore part of the tubes and in regions with minimum flow areas. The results, on the other hand, show smaller gradients of temperature in the dead air zone, with definite recirculation in the tube wake. This implies poor heat transfer in the dead air zone. The characteristic feature of the better heat transfer is attributable to the formation of a horseshoe vortex in front of the vertical tubes and prevailing heat convection in regions with smaller flow areas. The reasons for such heat-transfer enhancement will be given in Section 4.3. Like the fluid dynamic field variables, symmetry of the temperature field, with respect to $y = B/2$, remains for the conditions investigated and the geometry considered.

Figure 12 shows the temperature contours at some x–z planes. As this figure reveals, there is thermal boundary layer development along the fin-plate. These contours, as expected, are symmetric with respect to $z = H/2$, with gradients clustered primarily in regions in front of the tube.

4.3. Topological study of the flow structure in the flow passage

For a three-dimensional flow simulation, it is an enormous task to manage the tremendous amount of three-dimensional data. It is, in fact, practically impossible to sketch the associated flow structure except by using some approaches proposed in the literature. For a comprehensive introduction to these approaches, the reader is referred to Yates and Chapman [15].

4.3.1. Some topological bases. Of the possible methodologies that allow us to explore the kinematics of complex flows, we prefer the topological study of limiting streamlines. The rationale for this choice is that the flow structure can be best described by the topological properties

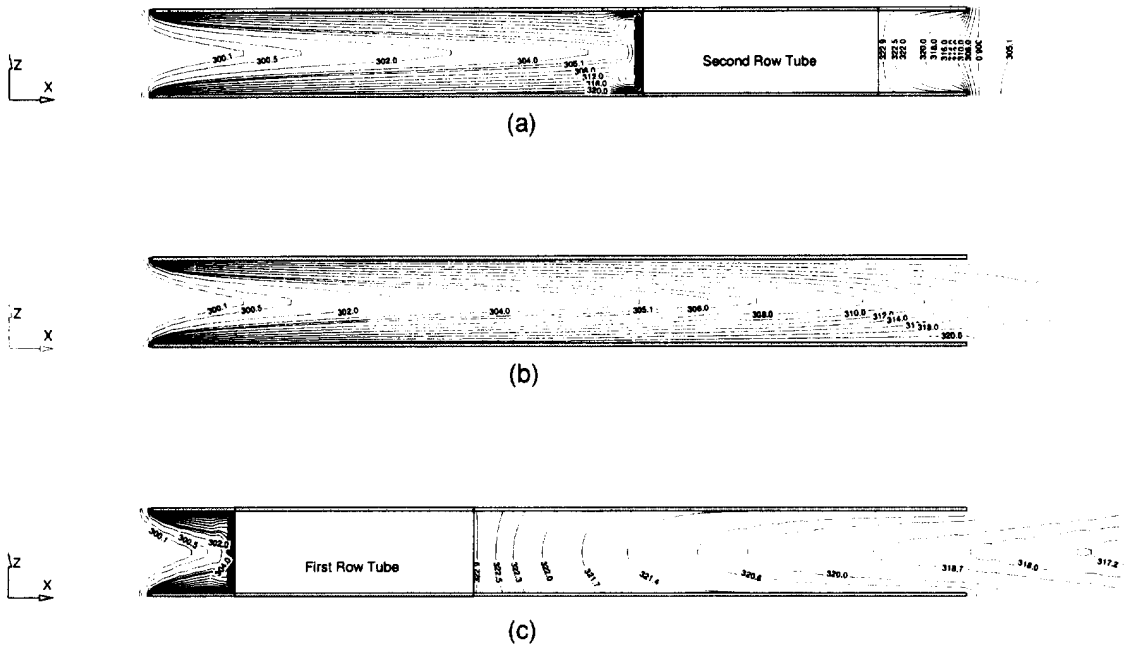

Fig. 12. Temperature contours at different y planes: (a) at the $y = 0$ plane; (b) at the $y = B/4$ plane; and (c) at the $y = B/2$ plane.

inferred from computed streamlines. Following Legendre [16], the study of the topology of three-dimensional streamlines projected onto a no-slip body surface is computationally analogous to the experimental surface flow visualization because the skin-friction line field, according to the definition of Lighthill [17], can be regarded as the projection of the three-dimensional streamline field onto the body surface. This implies that the observed topological patterns of limiting streamlines have significant implications for the flow evolution in the flow passage.

Kinematic aspects of computable limiting streamlines are best described in terms of singular points of different kinds. Determination of these singular points, from which the flow structure can be sketched, is thus important. In a set of velocity vectors, singular points are, by definition, classified as having zero magnitudes; therefore, their directions are indeterminate. Around a critical point, the vector field varies according to the eigenvectors and the eigenvalues of the Jacobian of the field at the detected critical point. Depending on the divergence of the shear-stress vector and the Jacobian just mentioned, singular points can be classified into two main topological types: nodal and saddle points [18]. Saddle points differ from nodes by their corresponding portraits. Passing through saddle points are only two shear-stress lines, on each of which the direction of the skin-friction vector field $[\mu(\partial u/\partial z), \mu(\partial v/\partial z)]$ changes sign on a surface z = constant. Depending on the type of saddle point, separation or attachment, both skin-friction directions point towards the critical point on one and both point away from this point on the other. This implies that saddle points act as barriers in the field of vectors. Nodal points, on the other hand, are classified as points through which an infinite number of shear-stress lines pass. Nodal points are of two types, namely, regular nodal points (or nodes) and foci (or spiral nodes). Nodal points of attachment act as sources of skin-friction lines that emanate from the point and spread out over the surface. Nodal points of separation, on the other hand, act as sinks where the skin friction lines circumscribing the body surface vanish. Foci and nodes differ in the orientation of their chosen vector field. For a singular point defined as a spiral node, all the shear-stress lines spiral onto or out of this point. Emanating from this type of node are two straight critical lines.

4.3.2. Flow topological inferred from the computed three-dimensional velocity vectors. With the underlying topological theory, some insight into the structure of the flow can be gained by examining the three-dimensional vector field. The motivation for undertaking topological study of the vector field was to classify some mechanisms that may aid heat-transfer capability. To provide a compact presentation here, in most of what follows the air with the inlet velocity $u_{in} = 2.5$ m/s will be considered.

To facilitate illustration of the topological structure of the flow, it is to first clarify the global structure of the fluid in the flow passage. To this end, we plot three-dimensional particle lines in some regions of physical importance in Fig. 13. As this figure shows, physical complexities are

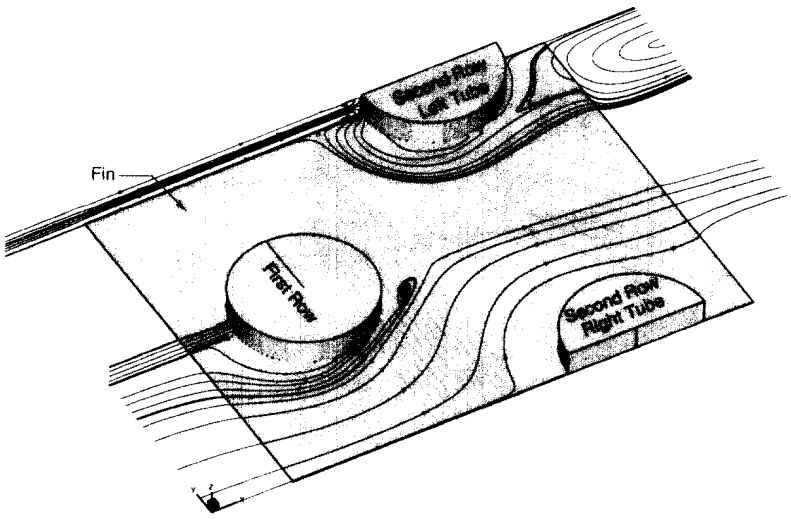

Fig. 13. A global picture of flow structure in the channel passage.

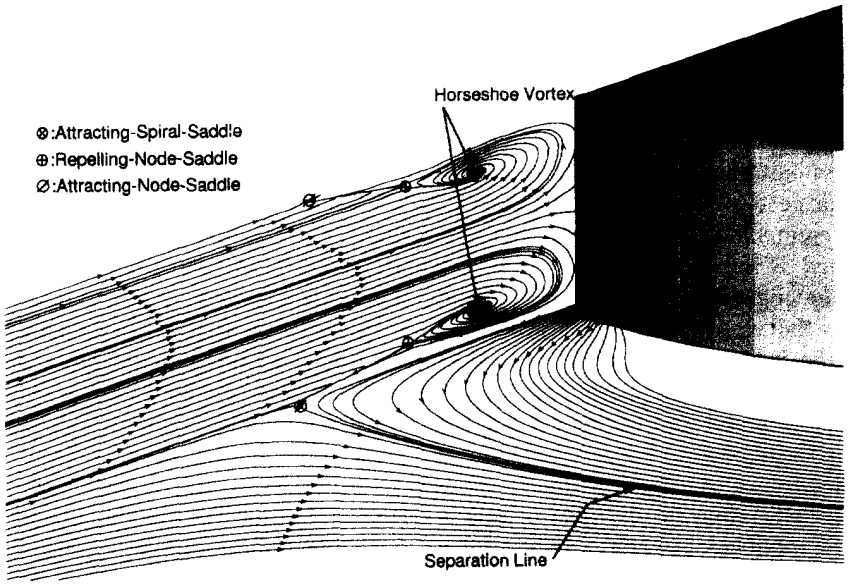

Fig. 14. An illustration of flow structure upstream of the second-row of the vortical cylinder.

observed in front of the tube. A better understanding of the local flow details helps us to improve heat-transfer rate of the existing heat exchanger. To achieve this goal, we plot in Fig. 14 streamlines in regions just in front of the second-row of tube as well as limiting streamlines on the fin surface. In Fig. 14, two sets of critical points which are symmetric with respect to the $z = H/2$ plane are clearly visible. By definition, in each class of critical points there exist three points labeled by different classifications as shown in Fig. 14. According to the classifications of critical points given in Section 4.3.1, we can classify the presence of horseshoe vortex points ahead of the cylinder tubes. These spiral saddle points can be found also at different Θ-cut planes, as shown in Fig. 15. A collection of horseshoe vortex points constitutes a global vortex core line. For particles released near this vortical core line, fluid particles should proceed along this line in a spiralling fashion. Horseshoe vortices which form in front of the tube near the bounded fin surfaces wrap around the tube and extend their journey to the rear of the tube. Due to the nature of horseshoe vortices, the spiralling motion adjacent to those vortex centers

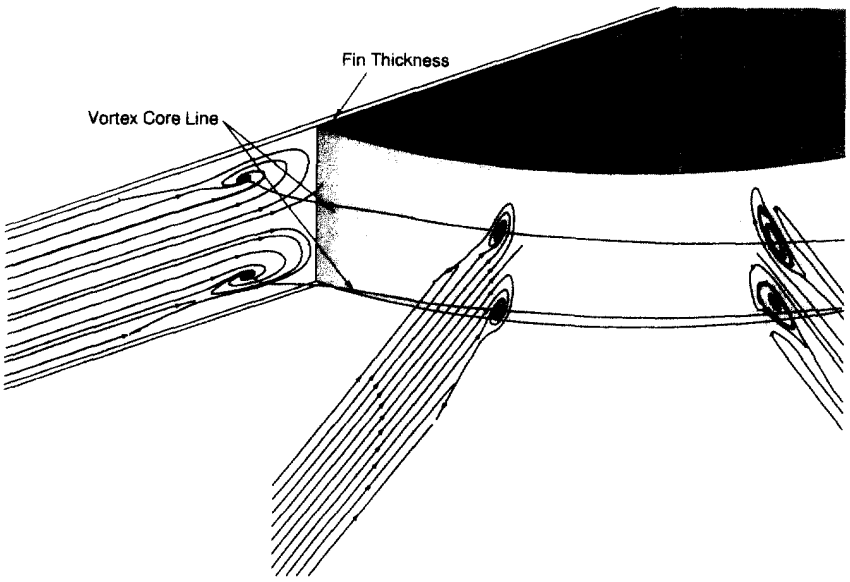

Fig. 15. An illustration of vortical core line in front of the second-row of the cylinder.

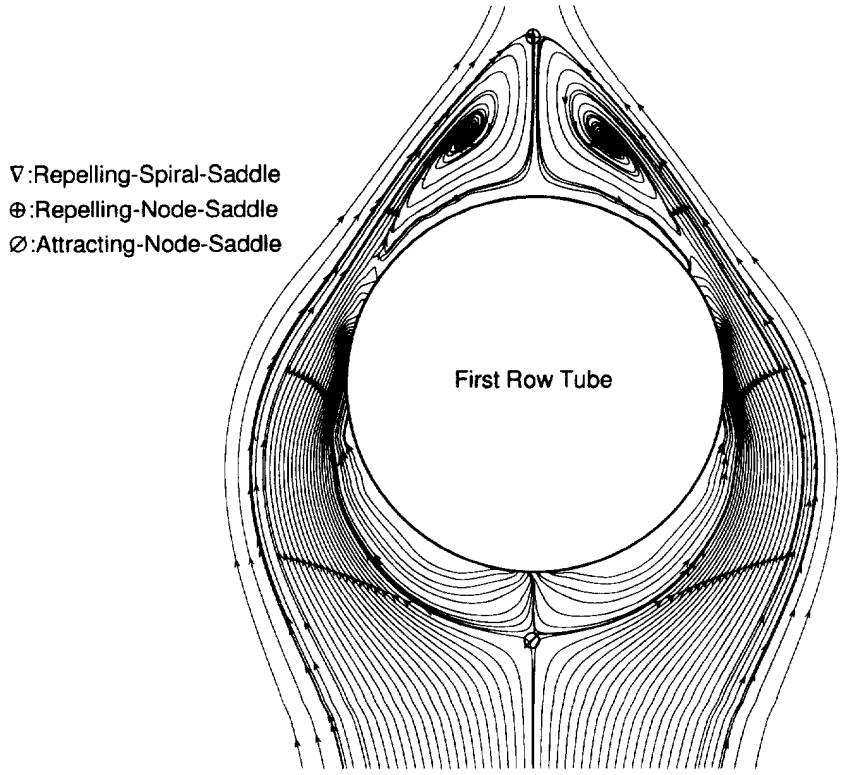

Fig. 16. Topological classification of singular points in regions around the first row tube.

enables good exchange of hot fluids in the tube with cold fluids in the main flow, thus ensuring good mixing of the fluid.

Further upstream of the horseshoe vortex point, there exists a critical point which is located on the fin surface. By definition, this spatial point is topologically labeled as the attracting-node-saddle. This implies that in regions near this point, flow moves towards this point. The other characteristic feature of the flow is flow separation near the apex of the tube. One can refer to Fig. 16 for confirmation of the above statement. Figure 16 also reveals the presence of

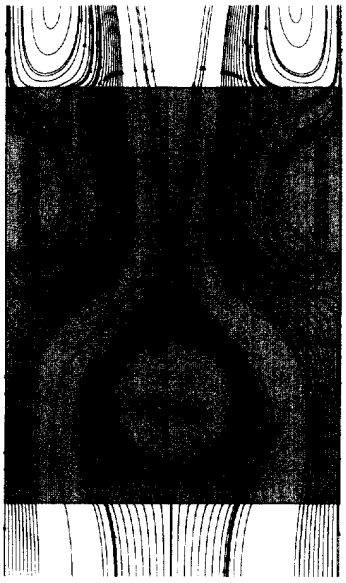

Fig. 17. Flow topology at the fin surface.

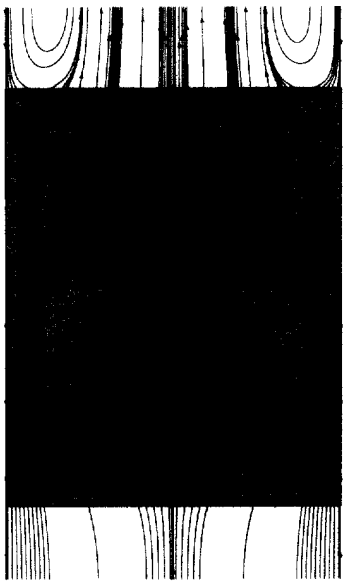

Fig. 18. Flow topology at the $z = H/4$ plane.

flow separation, which is typical for a flow past a circular tube. The flow separation is accompanied by formation of a tube wake within which fluid recirculates. This is mainly due to the accompanying dead air zone, which explains why the fin heat transfer is poor in the tube wake. A clear demonstration that the flow in the tube wake indeed recirculates is shown pictorially in Fig. 16. This formation of a tube wake has a strong association with the flow separation from the tube surface. For the main flow and wake flow configured as shown, we would expect to see a repelling critical point downstream of the wake. The flow structure in front of the second-row tube closely resembles that observed in the first-row tube. Readers are referred to Figs 17–19 for additional details. The shaded area indicates where the fin-plate is located. Due to space limitations, we do not plot the detailed flow structure ahead of the second-row tube; we instead concentrate our attention on regions behind the second-row tube. As Fig. 20 reveals, the flow also separates from the second-row tube but forms a different wake pattern. Weak critical points are found just behind the cylinder tube in the wake. The main reason for

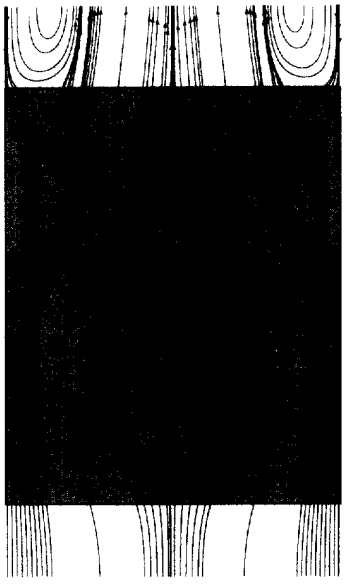

Fig. 19. Flow topology at the $z = H/2$ plane.

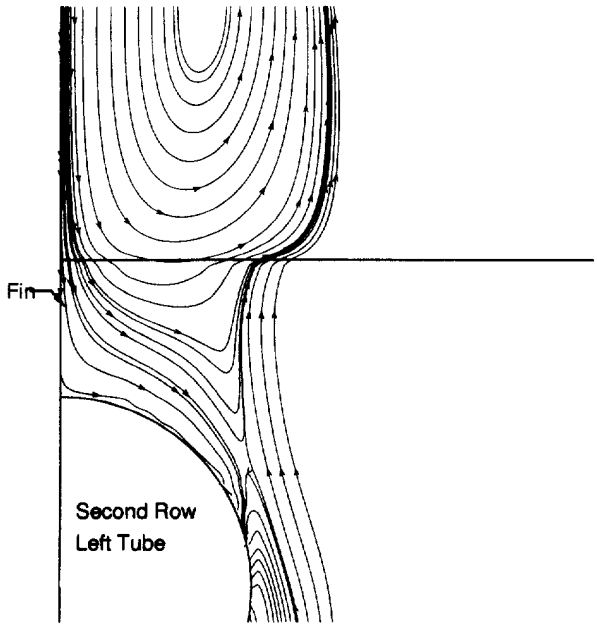

Fig. 20. Illustration of flow reversal downstream of the second tube.

the different wake pattern is the expansion flow behind the trailing edge of the fin-plate. It is this flow expansion that draws ambient air towards the flow passage. The area within the heavy dashed line, which is where recirculation from the ambient flow occurs, is possibly the regime where HTR may appear. According to Fig. 8, which plots the heat flux distribution:

$$\left(\dot{q} = -k\frac{\partial T}{\partial z}\bigg|_{z=0+}\right)$$

on the fin surface, the phenomenon of HTR is invisible for the case considered here. This figure is also important because it confirms that the horseshoe vortex assists the high heat transfer and that the wake behind the tube is the cause of the decreasing heat transfer.

5. CONCLUDING REMARKS

An investigation has been conducted to study the performance of a conjugate heat exchanger in dry conditions. The physical domain under investigation comprises two-row staggered cylinder tubes which are normal to two packed plane plates. For this study, test inlet velocities have been considered to study the effect of Reynolds number on the heat-transfer rate using a computer code which has been analytically and experimentally verified. Through this study, the topological theory is shown to be a useful tool for further details of the flow structure. The rather complex flow structure is depicted, and this broadens our knowledge of the implications of an interaction between horseshoe vortex and wake. This also explains how heat transfer is enhanced by the production of helical nature of the horseshoe vortex. Flow as well as heat transfer in the flow are also plotted to address the importance of the occurring vortical core line and the wake region just behind the cylinder.

Acknowledgements—The authors would like to acknowledge thanks to Fred P. C. Huang, H. H. Lin, J. Chien, J. Y. Lee, Y. C. Lin, J. H. Wu, W. M. Hu and C. P. Chiang in Teco Electric & Machinery Co., Ltd who have provided useful information in the course of this study.

REFERENCES

1. Tao, W. Q. and Lue, S. S., Numerical method for calculation of slotted-fin efficiency in dry conditions. *Numerical Heat Transfer, Part A*, 1994, **26**, 351.
2. Fiebig, M., Grosse-Gorgemann, A., Chen, Y. and Mitra, N. K., Conjugate heat transfer of a finned tube Part A: heat transfer behavior and occurrence of heat transfer reversal. *Numerical Heat Transfer, Part A*, 1995, **28**, 133.

3. Fiebig, M., Chen, Y., Grosse-Gorgemann, A. and Mitra, N. K., Conjugate heat transfer of a finned tube Part B: heat transfer augmentation and avoidance of heat transfer reversal by longitudinal vortex generators. *Numerical Heat Transfer, Part A*, 1995, **28,** 147.
4. Sparrow, E. M. and Chyu, M. K., Conjugate forced convection-conduction analysis of heat transfer in a plate fin. *Journal of Heat Transfer*, 1982, **104,** 204.
5. Grag, V. K. and Velusamy, K., Heat transfer characteristics for a plate fin. *Journal of Heat Transfer*, 1986, **108,** 224.
6. Rosman, E. C., Carajiescov, P. and Saboya, F. E. M., Performance of one- and two-row tube and plate fin heat exchanger. *Journal of Heat Transfer*, 1984, **106,** 627.
7. Biswas, G., Mitra, M. K. and Fiebig, M., Heat transfer enhancement in fin-tube heat exchangers by Winglet-type vortex generators. *International Journal of Heat and Mass Transfer*, 1994, **37**(2), 283.
8. Ladyzhenskaya, O. A., *Mathematical Problem in the Dynamics of a Viscous Incompressible Flow*. Gordon & Breach, New York, 1963.
9. Leonard, B. P., A stable and accurate convective modeling procedure based on quadratic upstream interpolation. *Computing Methods in Applied Mechanical Engineering*, 1979, **19,** 59.
10. Harlow, F. H. and Welch, J. E., Numerical calculation of time-dependent viscous incompressible flow of fluid with free surface. *Physics of Fluids*, 1965, **8,** 2182.
11. Abdallah, S., Numerical solution for the incompressible Navier-Stokes equations in primitive variables using a non-staggered grid II. *Journal of Computers and Physics*, 1987, **70,** 193–202.
12. Patankar, S. V., *Numerical Heat Transfer and Fluid Flow*. Hemisphere, New York, 1980.
13. Ethier, C. R. and Steinman, D. A., Exact fully 3D Navier–Stokes solutions for benchmarking. *International Journal of Numerical Methods in Fluids*, 1994, **19,** 369.
14. Chiang, T. P., Hwang, Robert R. and Sheu, W. H., Finite volume analysis of spiral motion in a rectangular lid-driven cavity. *International Journal of Numerical Methods in Fluids*, 1996, **23,** 325.
15. Yates, L. A. and Chapman, G. T., Streamlines, vorticity lines, and vortices around three-dimensional bodies. *AIAA Journal*, 1992, **30**(7), 1819.
16. Legendre, R., Séparation de courant lécoulement laminaire tridimensionnel. *Recherches Aéro*, 1956, **54,** 3.
17. Lighthill, M., *Attachment and separation in three-dimensional flow, in Laminar boundary layers*, ed. L. Rosenhead, Vol. II, pp. 72–82. Oxford University Press, 1963.
18. Tobak, M. and Peaks, D. J., Topology of three-dimensional separated flows. *Annual Review of Fluid Mechanics*, 1982, **14,** 61.